Zhang *et al. Energy Mater* 2024;4:400065
DOI: 10.20517/energymater.2024.25

Energy Materials

Article

Open Access

Check for updates

Interlayer expansion and conductive networking of MoS_2 nanoroses mediated by bio-derived carbon for enhanced potassium-ion storage

Shuo Zhang[1,#], Zonggui Yin[1,#], Lili Wang[1,*], Mengyao Shu[1], Xin Liang[1], Sheng Liang[1], Lei Hu[1], Chonghai Deng[1], Kunhong Hu[1], Xiaobo Zhu[2,*]

[1]Key Laboratory of Materials and Technologies for Advanced Batteries, LIB Technology Center of Anhui Province, Hefei University, Hefei 230601, Anhui, China.
[2]College of Materials Science and Engineering, Changsha University of Science and Technology, Changsha 410114, Hunan, China.
[#]Authors contributed equally.

***Correspondence to:** Dr. Lili Wang, Key Laboratory of Materials and Technologies for Advanced Batteries, LIB Technology Center of Anhui Province, Hefei University, Hefei 230601, Anhui, China. E-mail: wangll@hfuu.edu.cn; Dr. Xiaobo Zhu, College of Materials Science and Engineering, Changsha University of Science and Technology, Changsha 410114, Hunan, China. E-mail: xbzhu@outlook.com

How to cite this article: Zhang S, Yin Z, Wang L, Shu M, Liang X, Liang S, Hu L, Deng C, Hu K, Zhu X. Interlayer expansion and conductive networking of MoS_2 nanoroses mediated by bio-derived carbon for enhanced potassium-ion storage. *Energy Mater* 2024;4:400065. https://dx.doi.org/10.20517/energymater.2024.25

Received: 30 Mar 2024 **First Decision:** 8 May 2024 **Revised:** 10 Jun 2024 **Accepted:** 24 Jun 2024 **Published:** 2 Jul 2024

Academic Editor: Wei Tang **Copy Editor:** Fangling Lan **Production Editor:** Fangling Lan

Abstract

Potassium-ion batteries (PIBs) represent a promising battery technology for energy storage applications. Nevertheless, the progress of PIBs is still hindered by the lack of electrode materials that allow rapid and repeatable accommodation of the large K^+ ions. Herein, a composite anode material containing interlayered-expanded MoS_2 (55.6% larger) nanoroses in carbon nanonets (MoS_2/C@CNs) is designed with the assistance of biomass bagasse, of which the dual carbon sources convert into interlayer and skeleton carbon, respectively. The unique structure facilitates electron/ion transport in the entire electrode and offers excellent structural stability, leading to much improved electrochemical performance compared to simple MoS_2/C composite and pure MoS_2. Furthermore, the role of electrolyte salts (potassium hexafluorophosphate and potassium bis(fluorosulfonyl)imide) and the electrolyte concentration on the interfacial properties in PIBs have been explored. The results indicate that the low-concentration potassium bis(fluorosulfonyl)imide electrolyte helps to produce optimized organic-inorganic solid electrolyte interface films, contributing to a capacity retention of 90% after 1,000 cycles at 2 A g^{-1}.

Keywords: MoS_2, biomass, interlayer expansion, potassium-ion batteries, anode materials

© The Author(s) 2024. **Open Access** This article is licensed under a Creative Commons Attribution 4.0 International License (https://creativecommons.org/licenses/by/4.0/), which permits unrestricted use, sharing, adaptation, distribution and reproduction in any medium or format, for any purpose, even commercially, as long as you give appropriate credit to the original author(s) and the source, provide a link to the Creative Commons license, and indicate if changes were made.

INTRODUCTION

Electrochemical energy storage technologies are crucial for developing flexible sustainable energy systems. Among the emerging electrochemical energy storage technologies, potassium-ion batteries (PIBs) are promising to complement lithium-ion batteries (LIBs) owing to the rich potassium resources and their similar electrochemical properties to LIBs[1]. However, PIBs face challenges related to the large charge carrier of the K^+, rendering sluggish K^+ diffusion kinetics and low accommodation capacity in host electrodes[2]. Additionally, the considerable dimensional variations during (de)potassiation processes tend to cause structural damage of the host structures[3]. Therefore, designing capable electrode materials for efficient K^+ storage is critical.

Molybdenum disulfide (MoS_2) is an attractive anode material for PIBs due to its high theoretical capacity and a graphite-like layered structure featuring a wide interlayer spacing of 0.63 nm[4]. However, it suffers low conductivity, large dimensional change, and severe reconstruction during cycling, leading to inferior rate capability and fast capacity decay. Incorporating MoS_2 with nanocarbon can improve conductivity and suppress volume expansion[5-7]. Significant progress has been made in enhancing Li^+/Na^+ storage performance of MoS_2 using nanocarbon composites; the problems are still severe in K^+ systems due to the much larger ion size[8,9]. For example, while a MoS_2/graphite composite showed a high specific capacity for LIBs, its performance in PIBs was found to be significantly lower[10]. Therefore, the design of MoS_2/C composites with robust structures for efficient K^+ storage remains a significant challenge.

Previous research suggests that interlayer carbon can enhance electronic conductivity, suppress volume strain, and prevent the agglomeration of MoS_2. For instance, MoS_2-intercalated carbon hetero-layers[11], few-layer MoS_2 bonded with carbon[12], C/MoS_2/G Van der Waals (vdW) heterostructures[13] and expanded MoS_2 supported by N/O doped carbon[14] were investigated to have enhanced K^+ storage performance. Besides, building a three-dimensional (3D) charge transport network within the electrode using carbon structures such as a 3D graphene framework[15] or porous carbon skeleton[16,17] is another effective strategy for boosting K^+ storage performance, which offers feasible interconnected pathways for fast electron and ion transfer throughout the electrode.

Inspired by these considerations, here we design a MoS_2/C@CNs composite, where interlayer-expanded MoS_2/C nanoroses are embedded within a 3D carbon network derived from bagasse. The composite structure significantly improves electronic conductivity, reduces ion diffusion barriers, and limits MoS_2 aggregation. Furthermore, the uniform embedding of MoS_2/C nanoroses within the carbon nanonet facilitates electron/ion transport throughout the electrode and provides additional structural stability. We have further investigated the influence of different electrolyte salts (potassium hexafluorophosphate (KPF_6) and potassium bis(fluorosulfonyl)imide (KFSI)) and their concentrations on the electrode performance. MoS_2/C@CNs shows the best overall performance in 1M KFSI electrolyte, retaining a high capacity of 350 mAh g^{-1} at 200 mA g^{-1} after 400 cycles and 90% of its initial capacity after 1,000 cycles at 2 A g^{-1}. Our findings demonstrate that the high electrolyte concentration is not necessarily the best choice.

EXPERIMENTAL

Materials synthesis

Synthesis of MoS_2/AB

The MoS_2/activated bagasse (AB) precursor was prepared using a hydrothermal synthesis method. First, raw bagasse was added to the teflon hydrothermal reactor and stirred with 35 mL of 1 M KOH solution. This mixture was then oven-heated at 140 °C for 6 h. After cooling down, the solution was filtered using a funnel with deionized (DI) water and dried overnight to obtain KOH-AB. Next, 200 mg of AB, 1 mmol of

ammonium molybdate, and 4 mmol of thiocarbamide were added to the 30 mL of DI water, followed by being stirred for 30 min. Afterward, it was transferred to an autoclave and placed in an oven and heated at 200 °C for 18 h. Then, the hydrothermally reacted solution was centrifuged and washed thoroughly by DI water. After this, MoS_2/AB was obtained through freeze-drying to preserve the porous structure.

Synthesis of MoS_2/C@CNs

To prepare the final MoS_2/C@CNs, MoS_2/AB was calcinated at 700 °C for 2 h under Ar.

Synthesis of MoS_2/C and MoS_2

KOH-treated AB was annealed in Ar at 700 °C for 2 h to finalize the carbonization, creating a carbon sheet. Then, MoS_2/C was obtained by using the carbon sheet to support the hydrothermal growth of MoS_2. MoS_2 was also prepared without the carbon sheet.

Materials characterizations

Crystallinity of the materials was examined by an X-ray diffractometer (XRD, Rigaku Smart Lab SE) with Cu Kα radiation (λ = 1.54182 Å). A scanning electron microscope (SEM, JEOL JSM-7001F) and a transmission electron microscope (TEM, JEOL JEM-2010) were employed to investigate the morphologies and microstructures of the products. Surface area and porosity of the materials were analyzed by the Brunauer-Emmett-Teller (BET) method (Micromeritics TriStar II 3020). Vibrational spectra of the materials/electrodes were collected from a Fourier transform infrared (FT-IR, Thermo Nicolet 380) and a Raman (Horiba LabRAM HR Evolution, excitation wavelength of 532 nm) spectrometers. X-ray photoelectron spectroscopy (XPS, ESCALAB 250Xi) using a monochromatic Al Kα-excited light source was used to analyze the surface compositions and chemical valence states of the samples. The calibrated binding energy for C 1s is 284.8 eV. Thermogravimetric (TG) analyses were carried out on a thermal analyzer (TA instrument, Discovery TGA 550) under air at a heating rate of 10 °C min^{-1}.

Electrochemical measurements

First, 80 wt% active material, 10 wt% acetylene black, and 10 wt% polyvinylidene fluoride (PVDF) were mixed in the N-methyl-2-pyrrolidone (NMP) solution to form a slurry. The paste was then coated on the surface of a copper foil and vacuum-dried at 110 °C for 10 h. The dried electrode film was then cut into round discs. The electrode discs were assembled into CR2025 coin cells with potassium metal counter electrodes separated by glass fiber membranes. The solution of 1M KFSI in 1:1 (volume ratio) co-solvent of ethylene carbonate (EC) and diethyl carbonate (DEC) was employed as the standard electrolyte. Besides, different salts (KFSI, KPF_6) and concentrations were also investigated as the electrolytes. The fabricated cells were tested by cyclic voltammetry (CV) and electrochemical impedance spectroscopy (EIS) methods on an electrochemical potentiostat (Chenhua, CHI 760E). Galvanostatic charge/discharge and galvanostatic intermittent titration technique (GITT) measurements were conducted on a battery testing system (LAND, CT2001A). The electrolyte preparation and cell (dis)assembling were carried in an Ar-filled glovebox with oxygen and water levels below 0.5 ppm. All the electrochemical testing was conducted at room temperature (25 ± 2 °C).

RESULTS AND DISCUSSION

Figure 1A illustrates the synthesis process of the MoS_2/C@CNs composite materials. Firstly, bagasse is treated by KOH solution to dissolve the encapsulating hemicellulose and lignin. Then, MoS_2 nanostructures grow across the cellulose nanocrystals of AB via a hydrothermal reaction, where the carbohydrate molecules from AB tend to be trapped in the interlayers of MoS_2 nanosheets. The formation and evolution of MoS_2/AB composites during the hydrothermal reaction process have been investigated by tracking the time-

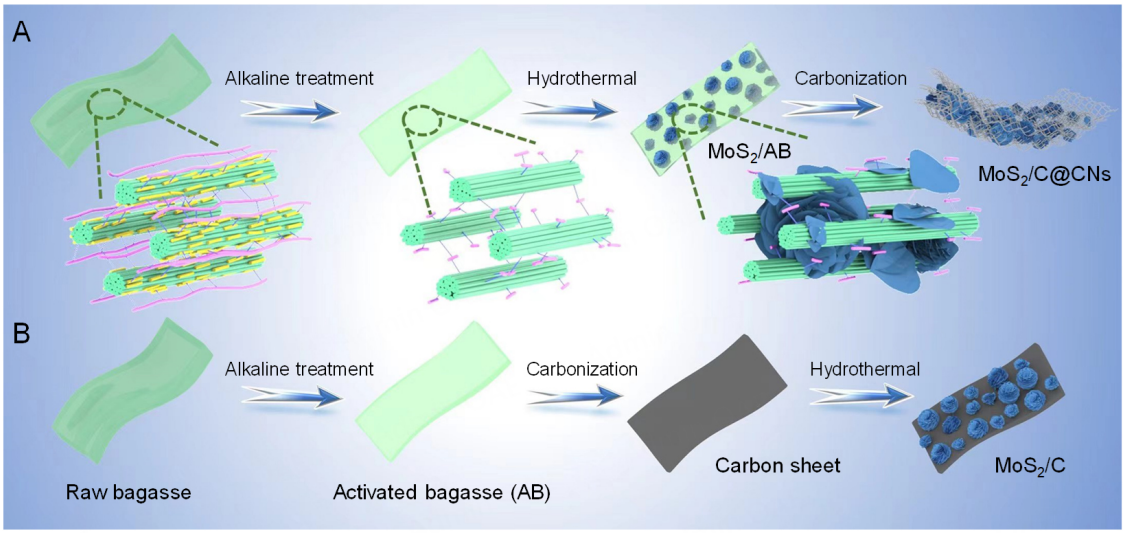

Figure 1. Schematic illustration of the synthetic procedures for (A) MoS_2/C@CNs and (B) MoS_2/C.

dependent products. Scanning electron microscopy (SEM) images [Supplementary Figure 1] record the morphological evolution of MoS_2/AB composites after different reaction durations. Accordingly, after 6 h, fine MoS_2 flakes nucleate on the AB matrix. These flakes grow gradually from six to 12 h and then self-assemble into flower-like structures on the AB matrix after 18 h. Meanwhile, XRD has been employed to understand the global structural evolution during the hydrothermal process. As shown in Supplementary Figure 2, the major peak at 22.1° is attributed to the (002) plane of cellulose II, a key crystalline component in bagasse. The (002) peak of MoS_2 at 8.4° emerges steadily and becomes observable after 6 h. Note that the AB-templated MoS_2 deviates significantly from standard peak location (about 13.9°) of MoS_2 at its presence, indicating the initial inclusion of carbohydrate molecules within the interlayers to form interlayer-expanded MoS_2. Finally, MoS_2/AB composite converts to MoS_2/C@CNs after calcination. In this process, the interlayer carbohydrate molecules transfer into carbon layers, forming interlayer-expanded MoS_2/C heterostructures. Simultaneously, due to the physical barrier provided by MoS_2, cellulose undergoes self-splitting into a carbon network during high-temperature carbonization. Consequently, a composite structure comprising MoS_2/C heterostructure anchored within the carbon network is obtained. For comparison, MoS_2/C is prepared via a route shown in Figure 1B, in which the AB is converted into carbon sheets before mixing with the molybdenum and sulfur precursors for the hydrothermal reaction. This difference leads to pristine MoS_2 nanoroses growing directly on the surface of the carbon sheet, lacking the crucial interlayer carbon in MoS_2/C@CNs.

Figure 2A displays the XRD patterns of the synthesized samples. The XRD patterns of the MoS_2/C and MoS_2 samples match well with the standard reference pattern for hexagonal MoS_2 (JCPDS 00-037-1492) without any impurity peaks. The main (002) peaks of both MoS_2/C and MoS_2 samples present at 13.85°, corresponding to a normal interlayer distance of 0.64 nm. In contrast, the (002) peak of MoS_2/C@CNs stands at a much lower angle of 9.02°. This suggests a massive interlayer expansion of 55.6% to 0.98 nm. These observations support the hypothesis that carbohydrate molecules are intercalated within the MoS_2 nanoroses during the hydrothermal reaction. These molecules then transform into a carbon layer during the subsequent calcination. Note that the absence of any distinct peaks associated with crystalline carbon suggests that the carbon matrix remains amorphous due to the relatively low calcination temperature. This is further supported by the Raman results [Supplementary Figure 3]. The characteristic E^1_{2g} and A_{1g} peaks of MoS_2 confirm its presence. The intensity ratio (I_D/I_G) of the D and G bands reaches a high value of 0.95,

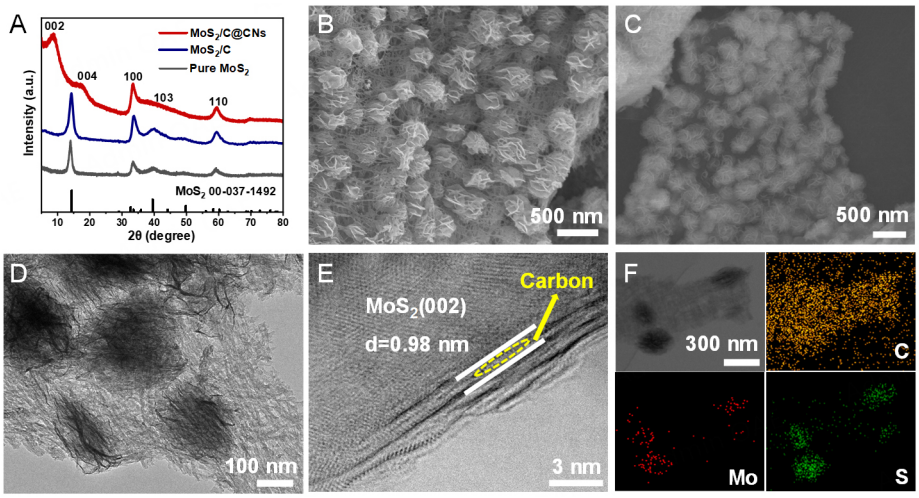

Figure 2. (A) XRD patterns of MoS_2/C@CNs, MoS_2/C, and pure MoS_2, (B) SEM image of MoS_2/C@CNs, (C) SEM image of MoS_2/C. (D and E) TEM and HR-TEM images of MoS_2/C@CNs. (F) TEM image and corresponding EDS mappings of C, S, and Mo.

confirming a low degree of graphitization. The abundant carbon defects in the samples offer additional active sites for efficient K^+ storage[14].

An SEM image of MoS_2/C@CNs [Figure 2B] reveals the highly dispersed MoS_2 nanoroses, consisting of thin sheets with a diameter of approximately 300 nm, are uniformly embedded within a 3D network of ultrafine carbon nanonets (diameter ~7 nm). These carbon nanonets, formed through carbonization of AB, provide several key functionalities. First, they can accommodate the dimensional variations of MoS_2 during charge/discharge cycles, enhancing its structural stability. Second, the close connection between MoS_2 and the nanonets forms a conduction structure, which facilitates electron and K^+ transport within the electrode. Figure 2C displays the SEM image of MoS_2/C. In comparison, the MoS_2 nanoroses in MoS_2/C are simply deposited on the surface of a smooth carbon sheet, lacking the intimate contact and 3D network. Transmission electron microscopy (TEM) characterization further reveals the intimate contact between MoS_2 nanoroses and the carbon nanonet in MoS_2/C@CNs [Figure 2D]. A high-resolution TEM (HR-TEM) image of MoS_2/C@CNs provides a detailed view of the MoS_2 microstructure within the composite [Figure 2E]. The interlayer spacing of MoS_2 is determined to be 0.98 nm, consistent with the XRD results. Notably, spots of sharp contrast can be observed between the MoS_2 layers, indicating the presence of interlayer carbon. These observations strongly support the hypothesis that during hydrothermal synthesis, carbohydrate molecules are embedded within the MoS_2 layers and transformed into interlayer carbon that supports the expansion of MoS_2. This unique MoS_2/C@CNs superstructure is expected to enhance the intrinsic ionic diffusivity in MoS_2 and improve structural stability by buffering volumetric strain during cycling. Although the MoS_2/C sample also has MoS_2 nanoroses on the carbon sheet matrix, as confirmed by TEM images [Supplementary Figure 4A and B], the absence of carbohydrate molecules in the calcinated carbon sheets results in the formation of MoS_2 structure with an interlayer distance of only 0.64 nm, according to the HR-TEM image [Supplementary Figure 4C]. In addition, energy-dispersive X-ray spectroscopy (EDS) elemental mappings of MoS_2/C@CNs [Figure 2F] confirm the composite structure by the clear elemental distributions, where Mo and S elements appear on the C matrix in a combined form.

Surface area and porosity of the synthesized materials have been characterized using BET analysis. As shown in Figure 3A, the isotherms of MoS_2/C@CNs belong to type-IV isotherms with H3-type hysteresis loops, signifying a well-developed mesoporous structure with slit-shaped pores formed by the

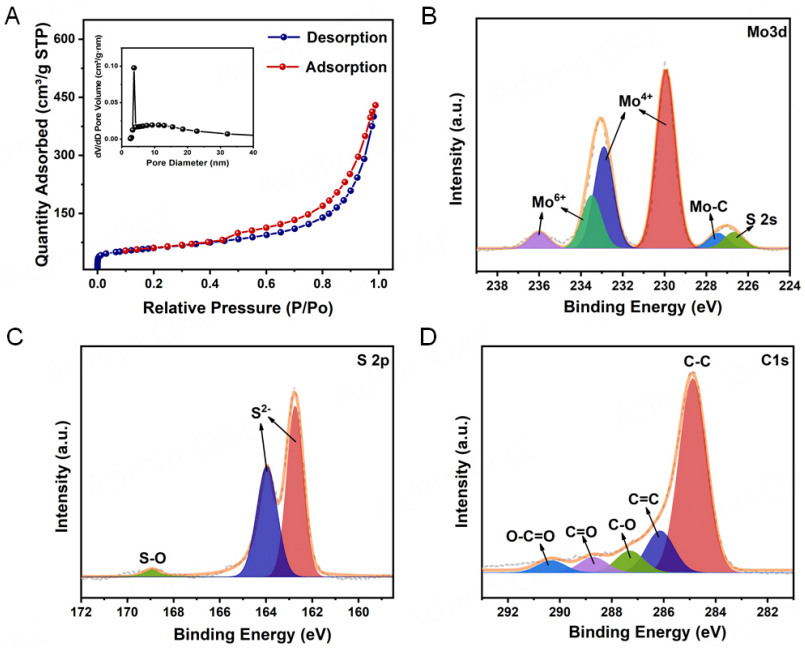

Figure 3. (A) N_2 adsorption-desorption isotherms of MoS_2/C@CNs, (B-D) XPS high-resolution spectra of Mo 3d (B), S 2p (C), and C1s (D) for MoS_2/C@CNs.

interconnected carbon nanonetwork[18]. The average pore size is 10.2 nm (inset in Figure 3A). The specific surface area of MoS_2/C@CNs reaches 210 $m^2 g^{-1}$. The mesoporous structure facilitates electrolyte infiltration and K^+ migration[19]. In contrast, the MoS_2/C sample has a lower specific area of 78.2 $m^2 g^{-1}$ and a smaller average pore size of 3.44 nm in Supplementary Figure 5.

XPS has been employed to measure the chemical states of Mo, S, and C in MoS_2/C@CNs. As shown in Figure 3B, the main peaks at binding energies of approximately 229.9 eV and 232.8 eV correspond to the doublet of Mo $3d_{5/2}$ and Mo $3d_{3/2}$ for Mo^{4+} oxidation station of MoS_2[20]. A pair of weaker peaks observed at around 236 and 233.4 eV can be attributed to Mo^{6+} $3d_{5/2}$ and Mo^{6+} $3d_{3/2}$ in MoO_3, due to surface oxidation of a small portion of molybdenum sulfide[13]. The S 2p spectrum of MoS_2/C [Figure 3C] consists of $2p_{3/2}$, $2p_{1/2}$ and S-O, located at 168.9, 163.9 and 162.7 eV[5]. The C 1s spectrum [Figure 3D] can be fitted into five peaks at 290.3, 288.7, 287.2, 286.1 and 284.8 eV, assigning to the O-C=O, C=O, C-O, C=C and C-C bonds, respectively[21-24]. Additionally, the carbon contents of MoS_2/C@CNs and MoS_2/C have been determined by TG analyses, as disclosed in Supplementary Figure 6. Accordingly, MoS_2/C@CNs and MoS_2/C have similar carbon contents, which are calculated to be 34.6 and 36.3 wt.%, respectively.

To assess the electrochemical mechanism of the composite materials, they have been fabricated into electrodes and assembled into half cells using potassium metal foils as the counter electrodes. Figure 4A presents the CV curve of the MoS_2/C@CNs electrode for the first three cycles with a scan rate of 0.1 mV s^{-1} in a voltage window of 0.01 to 3.0 V (*vs.* K^+/K). The reduction peak near 0.98 V in the initial cycle is associated with the insertion of K^+ with the MoS_2 layer to form K_xMoS_2[25]. Then, the intense peak centered at 0.56 V is due to the conversion reduction of K_xMoS_2 to the corresponding metal Mo and K_2S[4,10,13,26]. The growth of a solid electrolyte interface (SEI) layer from the reduction of the carbonate electrolyte also contributes to this peak, which weakens in the subsequent cycles[27]. The anodic peak at around 1.74 V suggests that the K^+ can be extracted from the electrode material[28]. To gain insights into the underlying potassium ion storage mechanisms, *ex-situ* XRD analysis has been performed [Supplementary Figure 7]. By

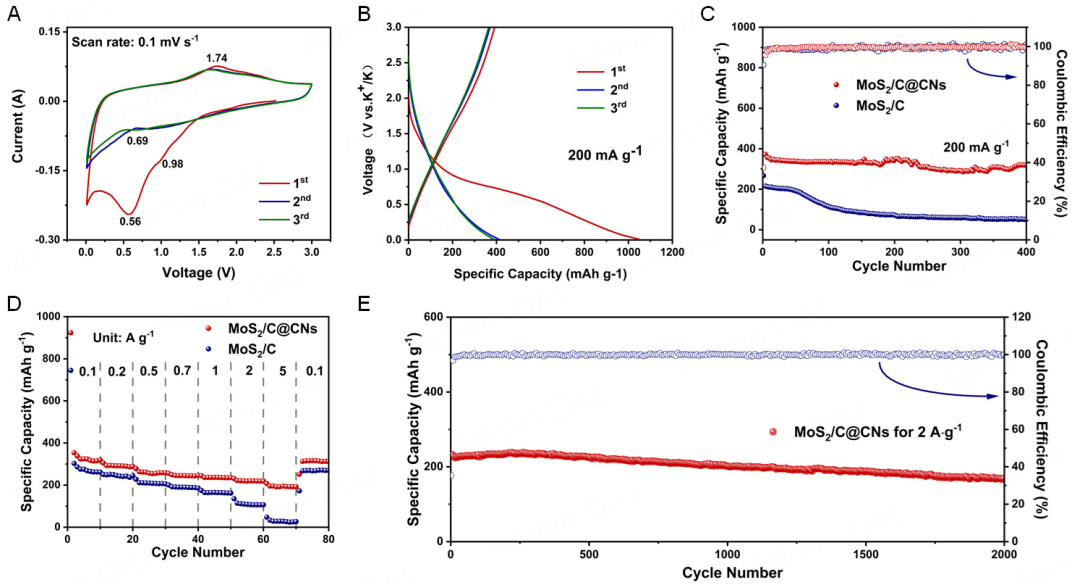

Figure 4. Electrochemical performance of MoS_2/C@CNs and MoS_2/C electrodes. (A) CV curves of MoS_2/C@CNs at 0.1 mV s^{-1}. (B) Discharge-charge profiles of MoS_2/C@CNs tested at 200 mA g^{-1}. (C) Cycling performance of MoS_2/C@CNs and MoS_2/C electrodes at 200 mA g^{-1}. (D) Rate performance. (E) Long-term cycle performance of MoS_2/C@CNs electrode at a high rate of 2 A g^{-1}.

examining the MoS_2/C@CNs electrode at different discharge states, it is evident that the (002) characteristic peak shifts from an initial angle of *ca.* 9.0° to *ca.* 6.3° upon discharging the electrode to the initial state to 1.2 V. This shift can be attributed to the insertion of potassium ions into the MoS_2 interlayer, resulting in the formation of K_xMoS_2 and consequently widened interlayer spacing. Afterwards, the peak position remains nearly unchanged upon further discharging, indicating the completion of insertion mechanism. Meanwhile, the (002) and (100) crystalline peaks of MoS_2 weaken gradually during discharging and dimmish at 0.01 V. This suggests that the conversion reaction that transforms MoS_2 into amorphous discharge products proceeds completely. The full completion of the conversion reaction indicates the potassium ion storage within the mesoporous architecture is kinetically favored, explaining the high accessible capacity.

Figure 4B displays the charge/discharge curves of the MoS_2/C@CNs electrode for the first three cycles at a current density of 200 mA g^{-1}. The initial discharge curve of MoS_2/C@CNs involves slight plateaus at 0.9 and 0.55 V, respectively, which are replaced by slope in subsequent cycles. The subsequent charge/discharge curves overlap very well, proving the excellent reversibility of the MoS_2/C@CNs electrode. The slope discharge profile indicates a pseudocapacitive behavior owing to (near-)surface charge storage[29]. The MoS_2/C@CNs electrode delivers a discharge capacity of 1,049 mA h g^{-1} and a charge capacity of 392 mA h g^{-1}, corresponding to an initial coulombic efficiency (ICE) of 37%. The low ICE can be explained by the formation of SEI film on the surface of MoS_2/C@CNs with a high surface area. In comparison, the MoS_2/C electrode shows a slightly higher ICE of 39.7% [Supplementary Figure 8] because of the calcinated carbon sheet matrix with a lower surface area and a reduced number of pores/defects, resulting in less SEI growth. Recently, the importance of ICEs of anode materials has gained attention. Strategies including prepotassization treatment[30], surface engineering[31], and electrolyte optimization[32] have been demonstrated to be effective in improving ICEs for future applications.

The cycling stability of the MoS_2/C@CNs and MoS_2/C electrodes is compared in Figure 4C. MoS_2/C@CNs retains a capacity of 350 mA h g^{-1} after 200 cycles at 200 mA g^{-1}, which is 95% of the third cycle capacity. Whereas the MoS_2/C electrode only delivers a specific capacity of 210 mA h g^{-1}, and the capacity drops rapidly to 110 mA h g^{-1} after 60 cycles. Moreover, the performance of pure MoS_2 electrodes has also been measured, which leaves only 63 mA g^{-1} after 200 cycles [Supplementary Figure 9A]. The rate performances of the electrodes have been further evaluated at different current densities [Figure 4D]. For MoS_2/C@CNs, the specific capacities reach 353, 305, 278, 256, 244, 231, and 207 mA h g^{-1} at the current densities of 0.1, 0.2, 0.5, 0.7, 1, 2 and 5 A g^{-1}, respectively. When the current density shifts back to 100 mA g^{-1}, a high capacity of 316 mA h g^{-1} can be retrieved. In contrast, MoS_2/C only shows capacities of 275, 238, 208, 191, 165, 115, and 34 mA h g^{-1} at current densities of 0.1, 0.2, 0.5, 0.7, 1, 2 and 5 A g^{-1}, respectively. Clearly, the advantage of MoS_2/C@CNs is much more evident under high rates. As anticipated, pure MoS_2 electrodes show the worst rate capability [Supplementary Figure 9B]. Furthermore, the long cycling performance of the MoS_2/C@CNs electrode has been further evaluated at a high current density of 2.0 A g^{-1}. As revealed in Figure 4E, it maintains a capacity of 164 mA h g^{-1} after 2,000 cycles, corresponding to an excellent retention ratio of 77.7%. These results confirm that the MoS_2/C@CNs electrode possesses an excellent potassium-ion storage property with enhanced electrochemical kinetics and reversibility, which are not only superior to the comparison sample but also advantageous compared to the other reported MoS_2 anode [Supplementary Table 1].

To further understand the K^+ storage mechanism and reaction kinetics, the capacitance contribution and K^+ diffusion coefficient (D_{K^+}) of MoS_2/C@CNs and MoS_2/C were evaluated by CV and GITT methods, respectively. Figure 5A records the CV curves of the MoS_2/C@CNs electrode at various scan rates from 0.1 to 3 mV s^{-1} in the voltage window of 0.01-3.0 V. The correlation between scan rate (v) and peak current (i) can be expressed by[33]:

$$i = av^b \tag{1}$$

This can be converted to:

$$\log i = b\log v + \log a \tag{2}$$

in which a and b are constants. When b approaches 0.5, the reaction is diffusion-controlled. When b reaches 1.0, capacitive behavior predominates[34]. By plotting log i against log v, clear linear relationships are observed [Figure 5B]. The slope b values of 0.80 and 0.78 indicate a significant pseudocapacitive contribution to potassium-ion storage. The capacitive contribution can be further quantified based on:[35]

$$i(V) = K_1v + K_2v^{1/2} \tag{3}$$

where the capacitive charge (K_1v) is calculated and illustrated as shaded zones inside the experimental CV curves [Supplementary Figure 10]. At 0.3 mV s^{-1}, the capacitance part accounts for 41% of the total charge storage. This proportion increases progressively with the enhancement of the sweep rate, ultimately reaching 50% at 1 mV s^{-1} [Figure 5C]. This trend indicates a significant shift towards capacitive behavior with increasing scan rates, highlighting the dynamic nature of charge storage mechanisms in the electrode material. In parallel, MoS_2/C has also been analyzed [Figure 5D]. Figure 5E shows the CV curves of the MoS_2/C at different scanning rates. The b values for MoS_2/C are 0.61 and 0.77 [Figure 5F], suggesting less pseudocapacitive effect. Correspondingly, Supplementary Figure 11 shows the shaded capacitive contributions at different scanning rates, which are further presented in Figure 5F. The capacitive

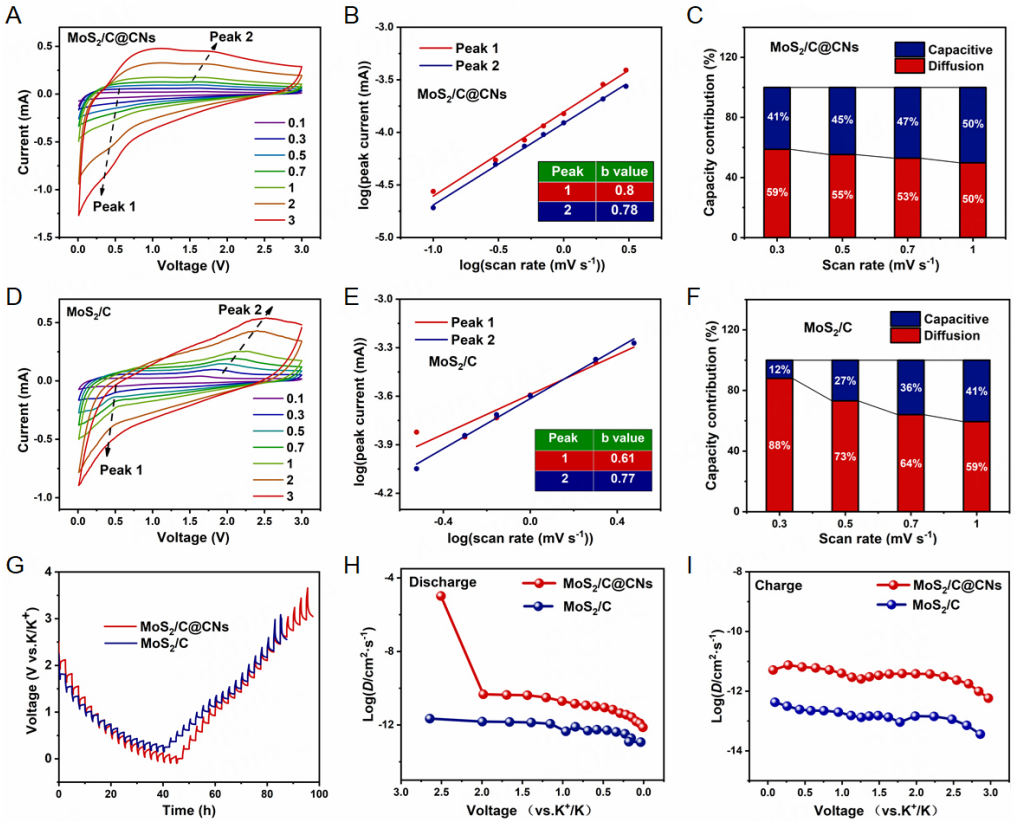

Figure 5. (A) CV curves at different scan rates from 0.1 to 3 mV s^{-1} for MoS_2/C@CNs electrode. (B) Determine the value of *b* using the relationship between peak currents and sweep rates. (C) Calculated capacitive and diffusion-controlled contributions to the total capacity under different sweep rates. (D-E) Same CV analyses for MoS_2/C electrode. (G) GITT voltage profiles for MoS_2/C@CNs and MoS_2/C electrodes. (H and I) K^+ diffusion coefficients calculated by GITT for MoS_2/C@CNs and MoS_2/C.

contribution is quantified to be only 12% at 0.3 mV s^{-1}. The diffusion-controlled contribution is found to be reduced much more severely compared to that of MoS_2/C@CNs. This also suggests a much higher diffusion barrier in MoS_2/C.

Figure 5G illustrates the GITT responses of electrodes with a pulse current of 50 mA g^{-1} for 30 min at 2 h rest intervals at the 10th cycle. D_{K+} can be calculated according to the Fick' second law[36]. According to the calculation results in Figure 5H and I, the average K^+ diffusion coefficient of MoS_2/C@CNs in the discharge and charging process is considerably higher than that of MoS_2/C, answering the enhanced rate capability of MoS_2/C@CNs. In addition, EIS spectra have been measured to compare the two electrodes after ten cycles [Supplementary Figure 12], and the fitted charge transfer resistance (R_{ct}) of MoS_2/C@CNs (1,054 Ω) is much lower than that of MoS_2/C (1,900 Ω).

Previous research suggests that the electrolyte significantly influences potassium storage performance[37]. In this regard, we have investigated how different potassium salts (KPF_6 and KFSI) and their concentrations affect the electrochemical performance of MoS_2/C@CNs electrodes in PIBs. Figure 6A compares the cycling stability of MoS_2/C@CNs electrodes cycled at 2,000 mA g^{-1} in four types of electrolytes: 1M KFSI, 6M KFSI, 0.8M KPF_6, and 6M KPF_6 (all in EC:DEC). After 1000 cycles, the electrode exhibits the best performance in 1M KFSI electrolyte, retaining a high reversible capacity of 210 mAh g^{-1} with 90% capacity retention. The cycling stability is significantly related to the concentration of the potassium salt. The specific capacity of the

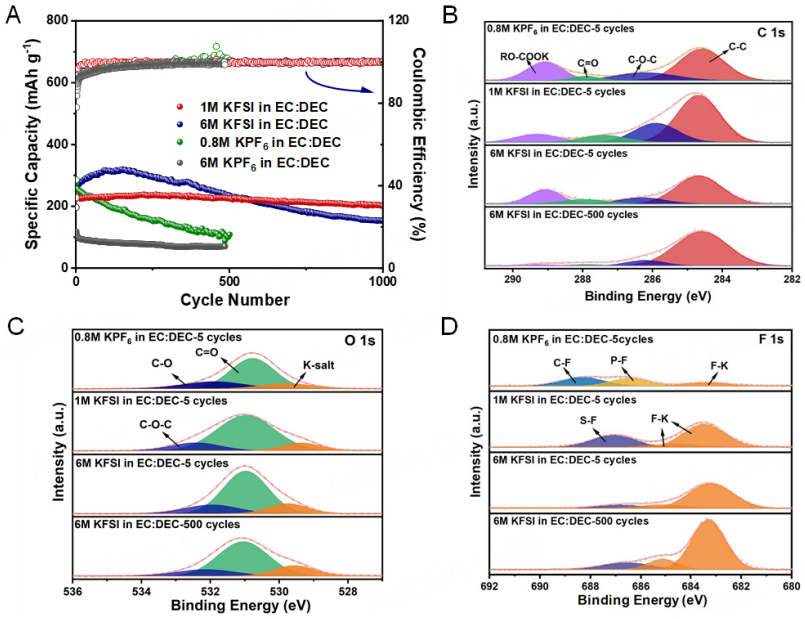

Figure 6. (A) Cycling performance of MoS_2/C@CNs electrode at 2,000 mA g^{-1} in 1M KFSI, 6M KFSI, and 0.8M KPF_6 in EC: DEC electrolytes. (B-D) XPS spectra of the fully discharged MoS_2/C@CNs electrodes after five cycles or 500 cycles in 0.8M KPF_6, 1M KFSI, and 6M KFSI electrolytes for C 1s (B), O 1s (C) and F 1s (D).

MoS_2/C@CNs electrode initially increases with cycling in the 6M KFSI electrolyte during the first 100 cycles. However, a sudden capacity fade is observed after 200 cycles. Whereas the electrode exhibits relatively poor performance in the 0.8M KPF_6 electrolyte, retaining only 98 mAh g^{-1} after 500 cycles with a capacity retention of just 38%. When cycled in the high concentration of 6M KPF_6 electrolyte, the initial capacity of the electrode reaches 275.7 mAh g^{-1} but decreases to only 70.9 mAh g^{-1} after 500 cycles. These results suggest a strong dependence of cell performance on both the type and the concentration of the electrolyte salt.

To understand the mechanism behind these performance variations, we have further analyzed the electrode-electrolyte interface of MoS_2/C@CNs electrodes cycled in the three different electrolytes using XPS. Figure 6B-D presents high-resolution C 1s, O 1s, and F 1s spectra for the electrodes after full discharge cycles (5th and 500th). The RO-COOK peak in the C 1s spectra is attributed to organic components in the SEI[20,38], while K-F represents the main inorganic component[39]. The RO-COOK peak in the C 1s spectra for the KFSI-based electrolyte is weaker than the KPF_6-based electrolyte. This suggests that the organic component of the SEI film formed under KPF_6 is higher, indicating less effective electrode passivation. Correspondingly, the F 1s spectra reveal a stronger inorganic K-F peak for the KFSI-based electrolyte compared to KPF_6. The high chemical stability, low solubility, and strong mechanical properties of K-F contribute to a more stable SEI layer[40-42]. These results suggest that the SEI film formed in the KPF_6-based electrolyte is less stable compared to the KFSI-based electrolyte, explaining the rapid cell degradation.

The influence of KFSI concentration has also been investigated by analyzing the composition of the SEI film for the MoS_2/C@CNs electrode cycled in 6M KFSI after five and 500 cycles. Interestingly, the C 1s spectrum shows a significant decrease in the organic component (RO-COOK) content after 500 cycles. In consistency, the F 1s spectrum manifests a substantial increase in the inorganic component (K-F) content after 500 cycles. While a thicker SEI film composed mainly of inorganic K-F salts can offer better mechanical stability and accommodate volume changes during cycling, an excessive amount can be detrimental[39,43,44]. As cycling proceeds, excessive inorganic salt deposition can lead to a thickened SEI layer with poor ionic conductivity

and lower efficiency, resulting in fast capacity decay observed during long-term cycling. This is further supported by the FT-IR [Supplementary Figure 13] and EIS results [Supplementary Figure 14]. Furthermore, high salt concentrations are suggested to cause irreversible collector corrosion in LIBs[45,46]. To explore the effect in PIBs, we have performed SEM characterization on the collector surface after 500 cycles in 1M and 6M KFSI electrolytes [Supplementary Figure 15]. Compared to the pristine collector, the surface after cycling in 1M KFSI shows slight corrosion, while the surface after cycling in 6M KFSI exhibits several large holes. This indicates that the high concentration of K-salt in 6M KFSI leads to more severe collector corrosion, contributing to irreversible capacity loss.

CONCLUSIONS

In summary, a MoS_2/C@CNs composite is synthesized and systematically characterized as an anode material for PIBs. A simple hydrothermal method followed by calcination is employed to create a 3D carbon network structure derived from biomass bagasse. This network not only facilitates electron transport but also buffers the volume expansion of MoS_2 during cycling. Simultaneously, the as-grown MoS_2 shows a few-layer structure with expanded (002) spacing supported by interlayer carbon, which accelerates K^+ ion diffusion. The as-prepared MoS_2/C@CNs electrode exhibits excellent electrochemical performance, achieving a reversible capacity of 342.5 mAh g^{-1} during the initial charge cycle. Furthermore, the electrode demonstrates remarkable cycling stability, retaining a specific capacity of 198 mAh g^{-1} after 2,000 cycles at 2 A g^{-1}. This exceptional performance is attributed to the synergistic effect of the 3D carbon network and expanded interlayer, which mitigates volume expansion and maintains structural integrity.

The influence of electrolyte type and concentration on the electrochemical performance has also been investigated. Our findings reveal that the type of potassium salt significantly affects the stability of the SEI layer. Electrolytes based on KPF_6 lead to the formation of an organic-rich SEI, hindering long-term cyclability. Conversely, KFSI-based electrolytes promote the formation of a more stable SEI with a higher content of inorganic K-F. However, excessively high concentrations of KFSI can lead to the formation of a thick SEI layer, compromising ionic conductivity and cycling performance. Additionally, high K-salt concentrations were found to accelerate collector corrosion. This study demonstrates that MoS_2/C@CNs composites prepared using a facile approach offer promising potential as anode materials for PIBs. By optimizing the electrolyte composition and concentration, the cycling stability and overall electrochemical performance can be significantly improved.

DECLARATIONS

Authors' contributions

Made substantial contributions to conception and design of the study and provided administrative, technical, and material support: Wang L, Zhu X
Performed data analysis and interpretation: Zhang S, Yin Z, Shu M
Performed data acquisition: Liang X, Liang S, Hu L, Deng C, Hu K

Availability of data and materials

Not applicable.

Financial support and sponsorship

This work was supported by the Key Projects for the Excellent Talent Foundation of Education Department of Anhui Province (No. gxyqZD2021136), the National Natural Science Foundation of China (52202210), Anhui Provincial Major Science and Technology Project (No. 2022e03020004), University Natural Science Research Project of Anhui Province (2022AH051788), the Team Projects Foundation of Education

Department of Anhui Province (2022AH010096), the Natural Science Foundation of Hunan Province (2024JJ5024), and the Scientific Research Fund of Hunan Provincial Education Department (22B0292).

Conflicts of interest

All authors declared that there are no conflicts of interest.

Ethical approval and consent to participate

Not applicable.

Consent for publication

Not applicable.

Copyright

© The Author(s) 2024.

REFERENCES

1. Rajagopalan R, Tang Y, Ji X, Jia C, Wang H. Advancements and challenges in potassium ion batteries: a comprehensive review. *Adv Funct Mater* 2020;30:1909486. DOI
2. Liu Q, Wang H, Jiang C, Tang Y. Multi-ion strategies towards emerging rechargeable batteries with high performance. *Energy Stor Mater* 2019;23:566-86. DOI
3. Wang B, Zhang Z, Yuan F, et al. An insight into the initial Coulombic efficiency of carbon-based anode materials for potassium-ion batteries. *Chem Eng J* 2022;428:131093. DOI
4. Liu S, Kang L, Henzie J, et al. Recent advances and perspectives of battery-type anode materials for potassium ion storage. *ACS Nano* 2021;15:18931-73. DOI
5. Wu H, Hou C, Shen G, et al. MoS_2/C/C nanofiber with double-layer carbon coating for high cycling stability and rate capability in lithium-ion batteries. *Nano Res* 2018;11:5866-78. DOI
6. Wang X, Tian J, Cheng X, Na R, Wang D, Shan Z. Chitosan-induced synthesis of hierarchical flower ridge-like MoS_2/N-doped carbon composites with enhanced lithium storage. *ACS Appl Mater Interfaces* 2018;10:35953-62. DOI
7. Zhao LP, Meng WS, Wang HY, Qi L. MoS_2-C composite as negative electrode material for sodium-ion supercapattery. *Acta Phys Chim Sin* 2017; 33:787-94. DOI
8. Sun W, Hu Z, Wang C, et al. Effects of carbon content on the electrochemical performances of MoS_2-C nanocomposites for Li-ion batteries. *ACS Appl Mater Interfaces* 2016;8:22168-74. DOI
9. Wang L, Zhang H, Wang Y, et al. Unleashing ultra-fast sodium ion storage mechanisms in interface-engineered monolayer MoS_2/C interoverlapped superstructure with robust charge transfer networks. *J Mater Chem A* 2020;8:15002-11. DOI
10. Li Y, Jiang S, Qian Y, et al. 2D interspace confined growth of ultrathin MoS_2-intercalated graphite hetero-layers for high-rate Li/K storage. *Nano Res* 2021;14:1061-8. DOI
11. Jia B, Yu Q, Zhao Y, et al. Bamboo-like hollow tubes with MoS_2/N-doped-C interfaces boost potassium-ion storage. *Adv Funct Mater* 2018;28:1803409. DOI
12. Guo J, Sun X, Shen K, et al. Controllable synthesis of tunable few-layered MoS_2 chemically bonding with in situ conversion nitrogen-doped carbon for ultrafast reversible sodium and potassium storage. *Chem Eng J* 2020;393:124703. DOI
13. Luo B, Wu P, Zhang J, et al. Van der Waals heterostructure engineering by 2D space-confinement for advanced potassium-ion storage. *Nano Res* 2021;14:3854-63. DOI
14. Zheng N, Jiang G, Chen X, Mao J, Zhou Y, Li Y. Rational design of a tubular, interlayer expanded MoS_2-N/O doped carbon composite for excellent potassium-ion storage. *J Mater Chem A* 2019;7:9305-15. DOI
15. Cao L, Zhang B, Xia H, et al. Hierarchical chrysanthemum-like MoS_2/Sb heterostructure encapsulated into N-doped graphene framework for superior potassium-ion storage. *Chem Eng J* 2020;387:124060. DOI
16. Cui Y, Liu W, Feng W, et al. Controlled design of well-dispersed ultrathin MoS_2 nanosheets inside hollow carbon skeleton: toward fast potassium storage by constructing spacious "houses" for K ions. *Adv Funct Mater* 2020;30:1908755. DOI
17. Lee JS, Park J, Baek KW, et al. Coral-like porous microspheres comprising polydopamine-derived N-doped C-coated $MoSe_2$ nanosheets composited with graphitic carbon as anodes for high-rate sodium- and potassium-ion batteries. *Chem Eng J* 2023;456:141118. DOI
18. Luo L, Dai J, Xia L, et al. An ultra-thin interlayer bimetallic sulfide for enhancing electrons transport of supercapacitor electrode. *J Energy Stor* 2022;55:105528. DOI
19. Yuan F, Zhang D, Li Z, et al. Unraveling the intercorrelation between micro/mesopores and K migration behavior in hard carbon. *Small* 2022;18:e2107113. DOI

20. Luo Z, Wang Y, Wang X, et al. Simultaneously engineering electron conductivity, site density and intrinsic activity of MoS_2 via the cation and anion codoping strategy. *ACS Appl Mater Interfaces* 2019;11:39782-8. DOI
21. Bai J, Zhao B, Zhou J, et al. Glucose-induced synthesis of 1T-MoS_2/C hybrid for high-rate lithium-ion batteries. *Small* 2019;15:e1805420. DOI
22. Wang J, Luo C, Gao T, Langrock A, Mignerey AC, Wang C. An advanced MoS_2 /carbon anode for high-performance sodium-ion batteries. *Small* 2015;11:473-81. DOI
23. Zhao X, Huang Y, Liu X, Yu M, Zong M, Li T. Magnetic nanorods/carbon fibers heterostructures coated with flower-like MoS_2 layers for superior microwave absorption. *Carbon* 2023;213:118265. DOI
24. Liu Y, Fan L, Jiao L. Graphene intercalated in graphene-like MoS_2: a promising cathode for rechargeable Mg batteries. *J Power Sources* 2017;340:104-10. DOI
25. Wu K, Cao X, Li M, Lei B, Zhan J, Wu M. Bottom-up synthesis of MoS_2/CNTs hollow polyhedron with 1T/2H hybrid phase for superior potassium-ion storage. *Small* 2020;16:e2004178. DOI
26. Ma G, Zhou Y, Wang Y, Feng Z, Yang J. N, P-codoped graphene supported few-layered MoS_2 as a long-life and high-rate anode materials for potassium-ion storage. *Nano Res* 2021;14:3523-30. DOI
27. He Y, Liu M, Huang Z, et al. Effect of solid electrolyte interface (SEI) film on cyclic performance of $Li_4Ti_5O_{12}$ anodes for Li ion batteries. *J Power Sources* 2013;239:269-76. DOI
28. Pramudita JC, Sehrawat D, Goonetilleke D, Sharma N. An initial review of the status of electrode materials for potassium-ion batteries. *Adv Energy Mater* 2017;7:1602911. DOI
29. Su X, Yu L, Cheng G, et al. Controllable hydrothermal synthesis of Cu-doped δ-MnO_2 films with different morphologies for energy storage and conversion using supercapacitors. *Appl Energy* 2014;134:439-45. DOI
30. Zhu Y, Wang M, Zhang Y, Wang R, Zhang Y, Wang C. Nitrogen/oxygen dual-doped hierarchically porous carbon/graphene composite as high-performance anode for potassium storage. *Electrochim Acta* 2021;377:138093. DOI
31. Liu Z, Han K, Li P, et al. Tuning metallic $Co_{0.85}Se$ quantum dots/carbon hollow polyhedrons with tertiary hierarchical structure for high-performance potassium ion batteries. *Nanomicro Lett* 2019;11:96. DOI PubMed PMC
32. Hosaka T, Matsuyama T, Kubota K, Yasuno S, Komaba S. Development of KPF_6/KFSA binary-salt solutions for long-life and high-voltage K-ion batteries. *ACS Appl Mater Interfaces* 2020;12:34873-81. DOI PubMed
33. Zhu X, Sun D, Luo B, Hu Y, Wang L. A stable high-power $Na_2Ti_3O_7$/$LiNi_{0.5}Mn_{1.5}O_4$ Li-ion hybrid energy storage device. *Electrochim Acta* 2018;284:30-7. DOI
34. Zhu X, She Q, Wang M, et al. Synchronous densification and conductivity modulation of nano-titanate for pseudocapacitive Li-ion storage. *Adv Funct Mater* 2024;34:2311025. DOI
35. Augustyn V, Simon P, Dunn B. Pseudocapacitive oxide materials for high-rate electrochemical energy storage. *Energy Environ Sci* 2014;7:1597. DOI
36. Dees DW, Kawauchi S, Abraham DP, Prakash J. Analysis of the galvanostatic intermittent titration technique (GITT) as applied to a lithium-ion porous electrode. *J Power Sources* 2009;189:263-8. DOI
37. Zhou J, Liu Y, Zhang S, Zhou T, Guo Z. Metal chalcogenides for potassium storage. *InfoMat* 2020;2:437-65. DOI
38. Li B, Zhao J, Zhang Z, et al. Electrolyte-regulated solid-electrolyte interphase enables long cycle life performance in organic cathodes for potassium-ion batteries. *Adv Funct Mater* 2019;29:1807137. DOI
39. Wang H, Zhai D, Kang F. Solid electrolyte interphase (SEI) in potassium ion batteries. *Energy Environ Sci* 2020;13:4583-608. DOI
40. Deng L, Zhang Y, Wang R, et al. Influence of KPF_6 and KFSI on the performance of anode materials for potassium-ion batteries: a case study of MoS_2. *ACS Appl Mater Interfaces* 2019;11:22449-56. DOI
41. Peng Y, Zhou W, Wang Z, et al. Regulating anion chemistry with F-containing bonds enable superior potassium ions storage in hard carbon. *Energy Stor Mater* 2023;62:102942. DOI
42. Wang Z, Luo K, Wu J, et al. Rejuvenating propylene carbonate-based electrolytes by regulating the coordinated structure toward all-climate potassium-ion batteries. *Energy Environ Sci* 2024;17:274-83. DOI
43. Allgayer F, Maibach J, Jeschull F. Comparing the solid electrolyte interphases on graphite electrodes in K and Li half cells. *ACS Appl Energy Mater* 2022;5:1136-48. DOI
44. Liu P, Wang Y, Hao H, et al. Stable potassium metal anodes with an all-aluminum current collector through improved electrolyte wetting. *Adv Mater* 2020;32:e2002908. DOI
45. Gabryelczyk A, Ivanov S, Bund A, Lota G. Taguchi method in experimental procedures focused on corrosion process of positive current collector in lithium-ion batteries. *Electrochim Acta* 2020;360:137011. DOI
46. Zhang L, Chai L, Zhang L, et al. Synergistic effect between lithium bis(fluorosulfonyl)imide (LiFSI) and lithium bis-oxalato borate (LiBOB) salts in $LiPF_6$-based electrolyte for high-performance Li-ion batteries. *Electrochim Acta* 2014;127:39-44. DOI